Feature Surfaces in Symmetric Tensor Fields Based on Eigenvalue Manifold

Jonathan Palacios, Harry Yeh, Wenping Wang, Yue Zhang, *Member, IEEE*,
Robert S. Laramee, *Member, IEEE*, Ritesh Sharma, Thomas Schultz, and
Eugene Zhang, *Senior Member, IEEE*

Abstract—Three-dimensional symmetric tensor fields have a wide range of applications in solid and fluid mechanics. Recent advances in the (topological) analysis of 3D symmetric tensor fields focus on degenerate tensors which form curves. In this paper, we introduce a number of feature surfaces, such as *neutral surfaces* and *traceless surfaces*, into tensor field analysis, based on the notion of *eigenvalue manifold*. Neutral surfaces are the boundary between linear tensors and planar tensors, and the traceless surfaces are the boundary between tensors of positive traces and those of negative traces. Degenerate curves, neutral surfaces, and traceless surfaces together form a partition of the eigenvalue manifold, which provides a more complete tensor field analysis than degenerate curves alone. We also extract and visualize the isosurfaces of tensor modes, tensor isotropy, and tensor magnitude, which we have found useful for domain applications in fluid and solid mechanics. Extracting neutral and traceless surfaces using the Marching Tetrahedra method can cause the loss of geometric and topological details, which can lead to false physical interpretation. To robustly extract neutral surfaces and traceless surfaces, we develop a polynomial description of them which enables us to borrow techniques from algebraic surface extraction, a topic well-researched by the computer-aided design (CAD) community as well as the algebraic geometry community. In addition, we adapt the surface extraction technique, called *A-patches*, to improve the speed of finding degenerate curves. Finally, we apply our analysis to data from solid and fluid mechanics as well as scalar field analysis.

Index Terms—Tensor field visualization, feature-based visualization, tensor field topology, traceless tensors, A-patches, scalar fields

✦

1 INTRODUCTION

THREE-DIMENSIONAL symmetric tensor fields have a wide range of applications in science, medicine, and engineering. Most earlier work focuses on semi-positive definite tensors, with the main application in medical imaging. More recent advances focus on the understanding and extraction of degenerate tensors in a tensor field. For example, Zheng et al. [1], [2] point out that under *structurally stable* conditions degenerate points form curves. Along a

- *J. Palacios and R. Sharma are with the School of Electrical Engineering and Computer Science, Oregon State University, 1148 Kelley Engineering Center, Corvallis, OR 97331.*
  E-mail: {palacijo, sharmrit}@eecs.oregonstate.edu.
- *H. Yeh is with the School of Civil and Construction Engineering, Oregon State University, 208 Owen Hall, Corvallis, OR 97331.*
  E-mail: harry@engr.oregonstate.edu.
- *W. Wang with the Department of Computer Science, The University of Hong Kong, Pokfulam Road, Hong Kong. E-mail: wenping@cs.hku.hk.*
- *Y. Zhang is with the School of Electrical Engineering and Computer Science, Oregon State University, 3117 Kelley Engineering Center, Corvallis, OR 97331. E-mail: zhangyue@onid.oregonstate.edu.*
- *R. S. Laramee is with the Department of Computer Science, Swansea University, SA2 8PP, Wales, UK. E-mail: R.S.Laramee@swansea.ac.uk.*
- *T. Schultz is with the Institute of Computer Science, University of Bonn, Friedrich-Ebert-Allee 144D-53113, Bonn, Germany.*
  E-mail: schultz@cs.uni-bonn.de.
- *E. Zhang is with the School of Electrical Engineering and Computer Science, Oregon State University, 2111 Kelley Engineering Center, Corvallis, OR 97331. E-mail: zhange@eecs.oregonstate.edu.*

degenerate curve the tensor field exhibits 2D degenerate tensor patterns such as wedges and trisectors [3]. Tricoche et al. [4] develop an efficient degenerate curve extraction method by noticing that degenerate curves in the tensor field are a subset of the ridge and valley lines of *mode*, a tensor invariant. All of these advances are inspirational to our research, for not only the insights they provide but also new and interesting questions they open.

For example, are degenerate tensors the only features in a tensor field? If not, what other features should be included in tensor field analysis, and why? What is the relationship among these features?

In searching for answers to these questions, our research leads to the notion of *eigenvalue manifold*, which shows that the set of *traceless* tensors and the set of *neutral tensors* (the medium eigenvalue equal to the average of the major and minor eigenvalues) are also important features in a tensor field. Across neutral surfaces, the predominant eigenvector field switches from the major eigenvector field to the minor eigenvector field. Together, neutral surfaces and traceless surfaces divide the domain into four types of regions, each of which has a unique characteristic.

Neutral surfaces are the zeroth levelset of tensor mode function, which is a trivariate polynomial in terms of spatial coordinates. Using the standard Marching Tetrahedra method [5] can lead to large errors in the geometry and topology of the neutral surfaces. To robustly extract neutral surfaces, we convert the problem of finding such features into the problem of finding algebraic surfaces, a well-researched topic in the computer-aided design and algebraic geometry communities. By adopting the idea of *A-patches*, based on
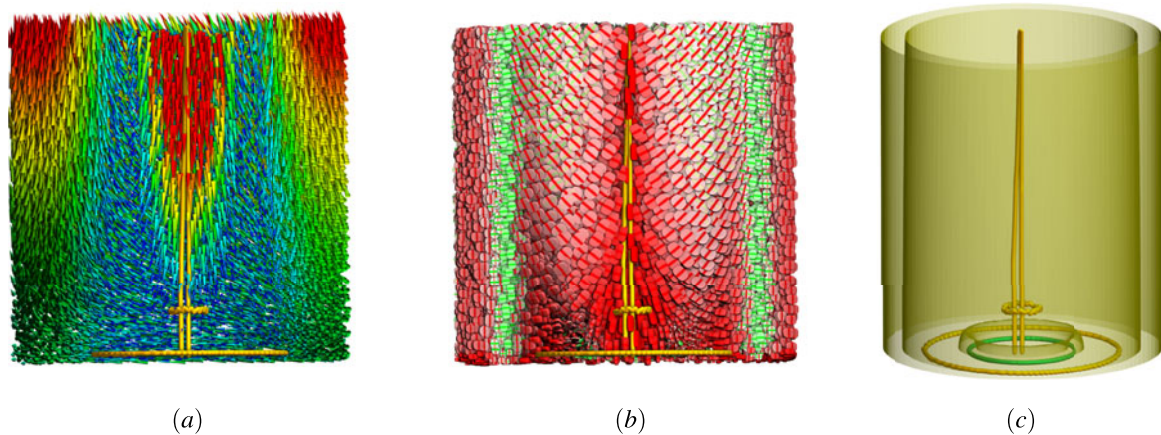
(a) (b) (c)

Fig. 1. This figure shows the results of applying our tensor field visualization to the Sullivan vortex: (a) the vector field shown in colored arrows supplemented with tensor field topology such as degenerate curves (colored curves), (b) our glyphs (Section 6: Fig. 5) based on the eigenvalue manifold (Section 4), and (c) neutral surfaces (chartreuse color) which separate linear degenerate tensors (green curves) and planar degenerate tensors (yellow curves).

Bernstein polynomials [6], neutral surfaces can be extracted with controlled topological errors. In addition, we make use of the idea of Bernstein polynomials to help improve the speed of degenerate curve extraction by first locating tetrahedra that do not contain degenerate curves and eliminating them from further processing.

We also extract and visualize the isosurfaces of tensor mode, magnitude, and isotropy. We have found that the transition of these surfaces over different isovalues can lead to insights into the domain applications.

We apply our analysis and visualization to data sets from solid mechanics and fluid dynamics and provide physical interpretations based on the analysis and visualization. Furthermore, we observe that tensor field analysis, when applied to the Hessian of a 3D scalar field, can provide critical information that is difficult to extract from existing scalar field visualization techniques.

In this paper we make the following contributions:

1) We introduce the notion of *eigenvalue manifold* for the analysis of 3D symmetric tensor fields, and include the set of neutral tensors and the set of traceless tensors into tensor field features. We also connect neutral tensors to tensor field topology through their interplay with degenerate tensors (Section 4).
2) We provide an efficient method to extract neutral surfaces and traceless surfaces, by reusing techniques from algebraic surface extraction. In addition, we speed up the degenerate curve extraction process based on Bernstein polynomials (Section 5).
3) We extract and visualize the isosurfaces of tensor mode, magnitude, and *isotropy index* (Section 4).
4) We provide physical interpretation of our analysis and visualization in the context of solid mechanics and fluid dynamics (Section 7).
5) We point out that tensor field analysis can provide critical insights into scalar field analysis (Section 7).

The rest of the paper is organized as follows. We review related work in Section 2 and relevant background on tensor fields in Section 3. We describe the theory of our tensor field analysis in Section 4. In Section 5 we provide a framework for robust extraction of feature surfaces as well as degenerate curves. We describe our visualization system in Section 6, including a set of glyphs that focus on showing tensor modes, i.e., traceless tensors. In Section 7 we show the results of applying our feature-based tensor field visualization to data sets from solid mechanics, fluid dynamics, as well as scalar field analysis. Section 8 summarizes our work and discusses limitations of our approaches as well as some possible future research directions.

2 PREVIOUS WORK

We start by reviewing relevant prior work on the topic of 3D tensor fields for scientific visualization. There has been much work on 2D tensor fields, and we refer the readers to [7], [8] and references therein. For 3D symmetric tensor fields, surveys on diffusion tensors from medical images can be found in [9], [10] while a survey on non-positive-definite tensors is available by Kratz et al. [11]. Much work on tensor field topology is inspired by topological analysis of vector fields, and the readers can find a good review of work in vector field topology in [12]. In this paper we will only review work most closely related to the present topic.

Delmarcelle and Hesselink [13] introduce the notion of hyperstreamlines for the visualization of 2D and 3D symmetric tensor fields. Hsu [14] and Zheng and Pang [15] visualize hyperstreamlines by adapting the well-known Line Integral Convolution (LIC) method of Cabral and Leedom [16] to symmetric tensor fields which they term *HyperLIC* [15]. Jankun-Kelly and Mehta [17] provide glyphs for traceless tensors arising from the study of nematic liquid crystals. Schultz and Kindlmann [18] extend ellipsoidal glyphs that are traditionally used for positive-definite tensors to *superquadric glyphs* which can be used for general symmetric tensors. Their glyph design is based on mapping the set of 3D symmetric tensors to a lune on a sphere representing possible eigenvalue compositions. Recall that a lune is a region on a sphere bounded by two intersecting great circles (a great circle divides the sphere into two equal halves). In our paper we use the same lune for our topological analysis. However, we partition the lune differently from Schultz et al. and

introduce the notion of traceless tensors and neutral tensors, which we incorporate into tensor field analysis.

Delmarcelle and Hesselink [13], [19] introduce the topology of 2D symmetric tensor fields as well as conduct some preliminary studies on 3D symmetric tensors in the context of flow analysis. Hesselink et al. later extend this work to 3D symmetric tensor fields [20] and study the degeneracies in such fields. Zheng and Pang [1] point out that triple degeneracy, i.e., a tensor with three equal eigenvalues, cannot be extracted in a structurally stable fashion. They further show that double degeneracies, i.e., only two equal eigenvalues, form lines in the domain. In this work and subsequent research [2], they provide a number of degenerate curve extraction methods based on the analysis of the discriminant function of the tensor field. Schultz et al. [21] point out the degenerate curve extraction methods of Zheng and Pang are often not adequate for real world data, such as those from medical imaging. Tricoche et al. [4] show that the degenerate curves in a tensor field are a subset of the ridge and valley lines of mode, a tensor invariant. They also develop a method to detect ridge and valley lines (degenerate curves) based on the parallel vector operator method [22]. In this paper, we introduce the notion of neutral surfaces and traceless surfaces, which we include in tensor field analysis and visualization.

In this paper we apply our analysis to a number of tensors arising from solid and fluid mechanics, including the stress tensors. Applying tensor field analysis to the stress tensor has been carried out recently by a number of visualization researchers [23], [24], with a focus on hyperstreamlines. In addition, we show that tensor field analysis can provide critical insights to scalar field analysis that is difficult to extract from existing scalar field visualization techniques.

3 TENSOR BACKGROUND

We review the relevant background on 3×3 symmetric tensors and tensor fields. This paper focuses on symmetric tensors. Consequently, in the remainder of the paper we will omit the mention of *symmetric* when referring to symmetric tensors. A 3×3 tensor T has three *real* eigenvalues $\lambda_1 \geq \lambda_2 \geq \lambda_3$, referred to as the *major eigenvalue*, *medium eigenvalue*, and *minor eigenvalue*, respectively. When the eigenvalues are mutually distinct, T is referred to as *non-degenerate*. In this case, it is possible to choose three unit eigenvectors $\{v_1, v_2, v_3\}$ such that v_i corresponds to λ_i for any $1 \leq i \leq 3$ and v_i's form a right-hand orthonormal basis of the space.

There are five important quantities derived from T that are invariant under the change of basis: (1) *trace*: $P = \lambda_1 + \lambda_2 + \lambda_3$, (2) *minor* $Q = \lambda_1\lambda_2 + \lambda_2\lambda_3 + \lambda_3\lambda_1$, (3) *determinant* $R = \lambda_1\lambda_2\lambda_3$, (4) *tensor magnitude*: $||T|| = \sqrt{\lambda_1^2 + \lambda_2^2 + \lambda_3^2}$, and (5) *mode* $M = \sqrt{6} \frac{(\lambda_1 - \frac{P}{3})^3 + (\lambda_2 - \frac{P}{3})^3 + (\lambda_3 - \frac{P}{3})^3}{[\sqrt{(\lambda_1 - \frac{P}{3})^2 + (\lambda_2 - \frac{P}{3})^2 + (\lambda_3 - \frac{P}{3})^2}]^3}$. A tensor can be uniquely decomposed as $\frac{P}{3}\mathbb{I} + A$ where $\mathbb{I}$ is the three-dimensional identity matrix and $A = T - \frac{P}{3}\mathbb{I}$ is referred to as the *deviator* of T. A is a *traceless* tensor, i.e., $P(A) = 0$. More importantly, the directional information (eigenvectors) in T is contained purely in its deviator in the following sense: a vector v is an eigenvector of T if and only if v is an eigenvector of A. In

fact, as we will discuss later, the *topology* of a tensor field can be defined in terms of its deviator tensor field. Another nice property of the set of traceless tensors is that it is closed under matrix addition and scalar multiplication, making it a linear subspace of the set of tensors.

We now consider *degenerate* tensors, which refer to tensors with repeating eigenvalues. There are three types of degenerate tensors: neutral ($\lambda_1 = \lambda_2 = \lambda_3$), linear ($\lambda_1 > \lambda_2 = \lambda_3$), and planar ($\lambda_1 = \lambda_2 > \lambda_3$). The neutral degeneracy is also referred to as the *triple degeneracy*, for which any non-zero vector is an eigenvector. The linear and planar degeneracies are called *double degeneracies*. The non-repeating eigenvalue is referred to as *non-degenerate eigenvalue*, while the repeating eigenvalues are referred to as the *degenerate eigenvalues*. Degenerate tensors can be described as the zeros of the so-called *discriminant*: $D = (\lambda_1 - \lambda_2)^2(\lambda_2 - \lambda_3)^2 (\lambda_3 - \lambda_1)^2 = Q^2P^2 - 4RP^3 - 4Q^3 + 18PQR - 27R^2$. Linear degenerate tensors have a mode value of 1, while planar degenerate tensors have a mode value of -1.

A *tensor field* is a continuous *tensor-valued* function in $\mathbb{R}^3$. A point **p** is a *(linear, planar, triple) degenerate point* if $T(\mathbf{p})$ is a degenerate tensor of the corresponding type. Given a generic tensor field, the set of triple degenerate points is structurally unstable, i.e., the structure does not persist under any arbitrarily small perturbation [25]. Under structurally stable conditions, linear and planar degenerate points form curves. The degenerate points on a degenerate curve must either be always linear or always planar. Moreover, a linear degenerate curve cannot intersect a planar degenerate curve because such an intersection point would be a triple degenerate point.

4 NOVEL TENSOR FIELD FEATURES AND EIGENVALUE MANIFOLD

Existing topological analysis of 3D symmetric tensor fields focuses on analyzing the behaviors of the tensor field around a degenerate curve. Such analysis is influenced primarily by the eigenvector analysis around individual degenerate curves. In this section, we introduce two new types of feature surfaces, the *neutral surfaces* (Section 4.1) and the *traceless surfaces* (Section 4.2). We also present the concept of *eigenvalue manifold* for symmetric tensors (Section 4.3), which integrates degenerate curves, neutral surfaces and traceless surfaces.

4.1 Neutral Surfaces

As we discussed earlier, along a linear degenerate curve, the major eigenvectors are well-defined, and the medium and minor eigenvectors are degenerate. Similarly, along a planar degenerate curve, the major and medium eigenvectors are degenerate, while the minor eigenvectors are well-defined. An interesting question is where the medium eigenvectors become *special*. The following theorem helps address this question.

Theorem 1. *Consider a continuous 3D symmetric tensor field $T(x, y, z)$ defined on a finite subvolume $\Omega \subset \mathbb{R}^3$. The major eigenvector field, a line field, can be converted into a continuous vector field on any simply-connected component $U \subset \Omega$ of the linear region in the tensor field, i.e., where $T(x, y, z)$ satisfies $\lambda_2 < \frac{\lambda_1 + \lambda_3}{2}$. Similarly, the minor eigenvector field of*

$T(x, y, z)$ can be converted into a continuous vector field inside a simply-connected component of the planar region in the tensor field, where $T(x, y, z)$ satisfies $\lambda_2 > \frac{\lambda_1 + \lambda_3}{2}$.

The proof is based on a classical result from differential topology [26] which states that a continuous line field on a differential manifold M is *orientable*, i.e., can be turned into a vector field consistently, if the line field has no singularities in M and the fundamental group of M contains no proper subgroups of order two. Since U is simply-connected, its fundamental group is *trivial*, i.e., containing only one element, the identity. Consequently, there is no element of order two in the group.

One significance of Theorem 1 is that the major and minor eigenvectors play different roles in regions where $\lambda_2 < \frac{\lambda_1 + \lambda_3}{2}$ (linear region) and regions where $\lambda_2 > \frac{\lambda_1 + \lambda_3}{2}$ (planar region). In the former, the minor eigenvector field contains all the interesting topological features in the tensor field (discontinuity in the eigenvector directions), while the major eigenvector field bears no topological significance. Transitioning into the latter type of region, the roles of the two eigenvector fields are reversed. The major eigenvector field now contains the topological features in the tensor field, while the minor eigenvector field is topologically insignificant. The boundary between these two types of regions, i.e., $\lambda_2 = \frac{\lambda_1 + \lambda_3}{2}$, or equivalently $\lambda_2 = 0$ if traceless, acts as the transition boundary between the major and minor eigenvector fields where their roles switch. We refer to such tensors as *neutral tensors*.

In a generic tensor field, the places where the tensor field is neutral form surfaces. We define the following descriptor:

$$N = \left(\lambda_1 - \frac{\lambda_2 + \lambda_3}{2}\right)\left(\lambda_2 - \frac{\lambda_3 + \lambda_1}{2}\right)\left(\lambda_3 - \frac{\lambda_1 + \lambda_2}{2}\right). \quad (1)$$

Then a tensor T is neutral if and only if $N = 0$. For traceless tensors, $N(T) = \frac{27}{8} R(T)$. Consequently, N is a multiple of the determinant of the deviator part of a tensor. It is straightforward to verify that a tensor is neutral if and only if its mode is zero. The eigenvalues of a neutral tensor have the form of $\lambda_0 + k$, λ_0, and $\lambda_0 - k$ for some $k \geq 0$. If the neutral tensor is also traceless, then its eigenvalues are k, 0, and $-k$.

The normal to the neutral surface at a given point $\mathbf{p}_0$ is the same as that of the neutral surface of its deviator tensor field. Assuming a traceless tensor field, this normal is then $\bigtriangledown R(T(\mathbf{p}_0)) = \bigtriangledown(\lambda_1 \lambda_2 \lambda_3)(\mathbf{p}_0) = \lambda_2(\mathbf{p}_0)\lambda_3(\mathbf{p}_0) \bigtriangledown \lambda_1(\mathbf{p}_0) + \lambda_3(\mathbf{p}_0)\lambda_1(\mathbf{p}_0) \bigtriangledown \lambda_2(\mathbf{p}_0) + \lambda_1(\mathbf{p}_0)\lambda_2(\mathbf{p}_0) \bigtriangledown \lambda_3(\mathbf{p}_0)$. Since $\lambda_2 = 0$ on neutral surfaces, the normal is simply $\bigtriangledown \lambda_2(\mathbf{p}_0)$. This suggests that the middle eigenvalue plays a special role at the neutral surface. It dictates both the location of the neutral surface ($\lambda_2 = 0$) and its normal ($\bigtriangledown \lambda_2$).

The above discussions, i.e., major and minor eigenvector fields switching roles at the neutral surface, and the medium eigenvalue playing a key role in deciding the location and normal of the neutral surface, inspire us to incorporate neutral surfaces into the topology of 3D symmetric tensor fields for the first time.

4.2 Isotropy Index and Traceless Surfaces

Given a tensor T and its trace-deviator decomposition $\frac{P}{3}\mathbb{I} + A$, the quantity $\phi = \arctan(\frac{P/3}{\|A\|})$ measures the ratio between the strength of the isotropy $\frac{P}{3}\mathbb{I}$ and the strength of the anisotropy A. For the stress tensor, $\|T\|$ is the total stress, while $\frac{P}{3}$ and $\|A\|$ are the *octahedral normal stress* and the *octahedral shear stress*, respectively. The octahedral shear stress is also called the von Mises stress [27]. When $\phi = \pm\frac{\pi}{2}$, $T = \frac{P}{3}\mathbb{I}$ is purely isotropic ($\pi/2$ for expansion and $-\pi/2$ for contraction) and when $\phi = 0$, $T = A$ is pure shear (purely anisotropic). We refer to ϕ as the *isotropic index*, a name inspired by the *shape index* [28], [29] for a 2×2 curvature tensor and is used to classify surface geometry into elliptical and hyperbolic sectors. Unfortunately, this quantity is not an algebraic function of the tensor entries. For robust surface extraction, we wish to find a quantity that can also characterize the ratio between isotropy and anisotropy in the tensor yet can lead to an algebraic expression. Consequently, we choose the quantity $\frac{P}{\sqrt{3}\|T\|}$ which has a range of $[-1, 1]$. We will refer to the latter formulation as the isotropy index in the remainder of the paper. The two quantities are equivalent in describing the isotropy and anisotropy ratios in the tensors because they can be expressed as monotonically increasing functions of the other quantity.

Given a generic tensor field, the set of points where the tensor field is traceless form surfaces. We refer to such surfaces as the *traceless surface*. While the trace of a tensor field is not affecting the eigenvectors of the tensor field, we wish to point out that the traceless surface represents significant change in the behavior of the tensor field. Therefore, we incorporate traceless surfaces into tensor field analysis along with neutral surfaces, which present transitions in the eigenvector fields (from rich in degenerate curves to free of degenerate curves and vice versa).

4.3 Eigenvalue Manifold

We now describe one model to characterize the behaviors of a tensor field, which we term *the eigenvalue manifold* of tensors. Consider the set of 3×3 tensors, which is a six-dimensional linear space. One of the simplifications of this space is to consider all possible eigenvalue combinations, i.e., $\{(\lambda_1, \lambda_2, \lambda_3) | \lambda_1, \lambda_2, \lambda_2 \in \mathbb{R}\}$. This is a three-dimensional linear space. The unit sphere in the space centering the origin is the set of unit tensors, i.e., unit tensor magnitude. However, there is a six-fold symmetry in this representation due to the permutations of λ_1, λ_2, λ_3. Consequently, it is sufficient to consider $\{(\lambda_1, \lambda_2, \lambda_3) | \lambda_1^2 + \lambda_2^2 + \lambda_3^2 = 1, \lambda_1 \geq \lambda_2 \geq \lambda_3\}$, which is a lune on the sphere $\{(\lambda_1, \lambda_2, \lambda_3) | \lambda_1^2 + \lambda_2^2 + \lambda_3^2 = 1\}$ bounded by two planes $\{(\lambda_1, \lambda_2, \lambda_3) | \lambda_1 = \lambda_2\}$ and $\{(\lambda_1, \lambda_2, \lambda_3) | \lambda_2 = \lambda_3\}$.

The aforementioned lune representation has been developed by Schultz and Kindlmann [18] to design glyphs for tensors with potentially negative eigenvalues. In their work, the lune is then divided into regions based on the sign of individual eigenvalues or their pairwise sums and differences.

In our analysis, we reuse the lune of Schultz et al. as the geometric representation of our eigenvalue manifold, but with a different parameterization (thus different analysis). Each point inside the eigenvalue manifold is characterized by two quantities: the tensor mode, and the isotropy index (Fig. 2 (top)). On any horizontal line, the tensor isotropy index remains constant, while the mode decreases from 1
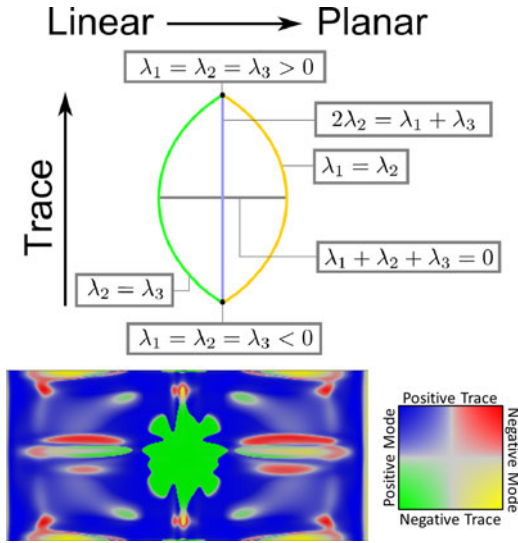
Fig. 2. The top of the figure shows the eigenvalue manifold, which is the shape of a lune. Notice that the same lune has been used by Schultz and Kindlmann [18] for the design of glyphs for indefinite tensors. The left and right parts of the lune's boundary correspond to linear degenerate tensors and planar degenerate tensors, respectively. The vertical bisector corresponds to the set of neutral tensors while the horizontal bisector corresponds to the set of traceless tensors. The corner points of the lune correspond to triple degenerate points. There are two types of such points, one with a positive trace, and the other with a negative trace. The two bisectors divide the eigenvalue manifold into four regions, representing different tensor behaviors. The bottom image shows the four-way partition of the eigenvalue manifold by neutral tensors and traceless tensors. The partition is demonstrated on a tensor field (bottom), which is the Hessian of the von Mises stress of a simulation data (Fig. 7: left).

Fig. 3. This figure compares the neutral surface of the three ball simulation using the Marching Tetrahedra method (top) and the A-patches method (bottom). Notice that not only does the A-patches method better preserve geometry details such as the outline of the holes, it also reduces the topological errors caused by the Marching Tetrahedra method.

(left boundary representing linear degenerate tensors) to -1 (right boundary representing planar degenerate tensors). The vertical bisector consists of neutral tensors. The top and bottom tips of the lune represent pure positive isotropy and pure negative isotropy, respectively. Travelling along the strictly descending path from the highest point to the lowest point in the lune, the isotropy index decreases, and one observes initially pure material expansion, followed by a mix of material expansion and shear deformation, pure shearing, a mix of material contraction and shear deformation, and finally pure material contraction. The horizontal bisector of the lune corresponds to traceless tensors. We wish to also comment that given a generic tensor field, the highest and lowest points in the lune are not possible, since they represent triple degenerate points that are structurally unstable. This implies that in material deformation, a pure expansion or contraction is structurally unstable as some shear deformation must occur.

The two bisectors (neutral tensors and traceless tensors) partition the lune into four parts of equal size (Fig. 2 (top)), based on the mode and trace of the tensor: (1) positively-traced linear tensors in the upper-left region, (2) positively-traced planar tensors in the upper-right region, (3) negatively-traced linear tensors in the lower-left region, and (4) nega-tively-traced planar tensors in the lower-right region. Fig. 2 (bottom) shows the result of applying this partition to a 3D tensor field. Each partition is given a unique color. Note that a positively-traced linear region cannot border a negatively-traced planar region. Similarly, a positively-traced planar region cannot border a negatively-traced linear region. The

notion of the eigenvalue manifold has been developed for 2D asymmetric tensor fields [8].

In our visualization system, we extract isosurfaces of ten-sor mode, tensor isotropy index, and magnitude, which we have found to be useful in our physical interpretations of various applications (Section 7).

5   FEATURE EXTRACTION METHODS

In this section we describe our method to extract neutral surfaces, traceless surfaces, and degenerate curves.

Marching Tetrahedra is a well-known technique to extract the levelsets of a function defined over a tetrahedral mesh. However, it assumes that the function is linear, which implies that if the function values at the two vertices of an edge have different signs, there must be one and exactly one zero crossing on the edge. Furthermore, if a tetrahedron intersects with a plane, then the plane must also intersect some edges of the tetrahedron, i.e., no plane can be completely enclosed by the tetrahedron. For the levelsets of non-linear functions, these assumptions do not hold, and errors in the surface topology can be uncontrolled. A state-of-the-art technique developed by the CAGD and algebraic geometry communities, called *A-patches*, provides a remedy to the problem [6]. Fig. 3 shows a comparison of the two methods for a simulation data set (Section 7).

In this paper, we incorporate the use of the A-patches method to extract neutral surfaces and traceless surfaces. In addition, we make use of the fundamental idea behind the *A-patches* to speed up the process of finding degenerate curves.

Given a polynomial function f and a tetrahedron t, the *A-patches* approach seeks to answer the following questions: does the zero levelset of f intersect t. If so, does it intersect t with a single sheet, and whether the single sheet is triangular

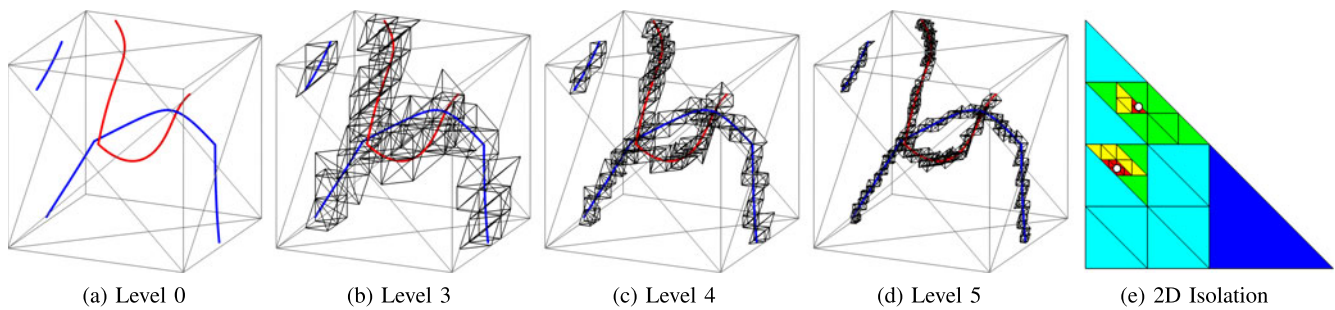| (a) Level 0 | (b) Level 3 | (c) Level 4 | (d) Level 5 | (e) 2D Isolation |

Fig. 4. Our framework based on *A-patches* can cull out tetrahedra not containing degenerate curves (a-d). In addition, on each face of a tetrahedron containing degenerate curves (e: the largest triangle), our method finds sub-regions on the face that can intersect with degenerate curves (e: the sub-triangles). The combination of tetrahedron culling and efficient search inside faces makes our degenerate curve extraction faster.

or quadrangular? The main idea behind the answers to these questions is the conversion of the polynomial of three variables (x, y, z) to the *Bernstein polynomials* of four variables $(\alpha, \beta, \delta, \gamma)$ where α, β, γ, and δ are the barycentric coordinates of points inside the tetrahedron t. The degree of polynomial f, denoted by $n = degree(f)$, gives rise to a set of control points (see [6] for an illustration of the control grid). The number of control points on each edge of t is $n + 1$. The properties of Bernstein polynomials ensure that if the function f has the same sign at two adjacent control points, then there are no zero crossings on the edge connecting them. If the signs are different, then there is exactly one zero crossing. Moreover, if a sub-tetrahedron formed by mutually adjacent control points have the same sign, then there cannot be a zero levelset of the polynomial surface in the interior of the sub-tetrahedron. In other words, by using the Bernstein polynomials, we are able to develop a grid inside the tetrahedron such that the properties of the Marching Tetrahedra method for linear functions are obtained, even when the function is not linear. Moreover, there is no need to perform random subdivision and search, as the degree of the polynomial produces the grid that guarantees the success of the *A-patches* method. The only exceptions to this are the singularities of the surfaces, which require additional subdivision.

At a high-level, the *A-patches* algorithm considers a few cases. In the first case, all the control points in the grid have the same sign. In this case there is no zero levelset inside the tetrahedron t. In the second case, there is a separating layer in the grid such that the control points on one side of the layer have one sign and the control points on the other side of the layer have the opposite sign. In this case there is a single sheet of zero levelset surface which can be extracted in a similar fashion to the Marching Tetrahedra method. If one side contains one vertex of the original tetrahedron and the other side contains three vertices of the tetrahedron, the surface is a triangular sheet. If each side contains two vertices of the tetrahedron t, then there is a quadrangular sheet of the surface. In the last case where the control points have mixed signs but no separating layer can be found or there are more than one separating layer, the tetrahedron is subdivided, and the process repeats for each tetrahedron in the subdivision.

Notice that the neutral surface and the traceless surface are both polynomials in terms of the components of the tensor fields, which are polynomials in terms of the 3D coordinates.

Besides extracting neutral surfaces, we have found the idea of *A-patches* useful for improving the degenerate curve extraction method. Existing techniques [1], [4] rely on finding the intersections of degenerate curves with the faces of the cells. Since there may be more than one degenerate curve intersecting a face, the techniques perform iterative subdivisions of the face in order to find all such intersections. However, it is difficult to predict where the intersection points are on the faces. Consequently, the face needs to be subdivided uniformly several times, without a clear stopping criterion. Moreover, even if no intersections have been found on any face of a cell, it is uncertain whether degenerate curves intersect the cell. Numerical issues are known to cause missing solutions in root-finding.

We adapt the *A-patches* idea to help address these issues. Recall that degenerate curves are the solutions to $D = 0$ where D is the discriminant of the tensor and is a degree-six polynomial in terms of the tensor entries. D can be expressed as the sum of squares of seven polynomials, each of which can be both positive and negative. Moreover, as long as one of the seven functions is purely positive (or negative) inside a tetrahedron, the discriminant will be strictly positive inside the tetrahedron, i.e., no degenerate curves. Therefore, for each tetrahedron t, we perform the *A-patches* algorithm on all seven functions. A tetrahedron or a sub-tetrahedron is eliminated as soon as all of the control points have the same sign for at least one function. This helps us quickly eliminate the tetrahedra that cannot contain degenerate curves. Next, for tetrahedra that intersect degenerate curves, we run the *A-patches* algorithm on each face of the tetrahedron, again using the seven functions. This allows us to efficiently identify regions in the face that intersect degenerate curves. Once we find these regions on the face, we resort back to the method of Zheng and Pang [1] by first searching for a zero point in each region and then connecting these points through tracing degenerate curves. Fig. 4 shows our method for both finding tetrahedra and sub-tetrahedra enclosing degenerate curves (a-d) and locating regions in the faces of tetrahedra that intersect degenerate curves (e).

6 VISUALIZATION TECHNIQUES

Our tensor field visualization system visualizes the features and topology of 3D symmetric tensor fields by depicting its degenerate curves, traceless surfaces, and neutral surfaces. In addition, one can inspect the behavior of the tensor field
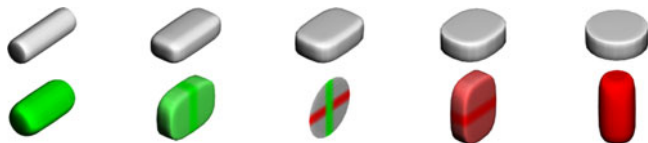
Fig. 5. A visual comparison of the superquadric glyphs (top) and our glyphs (bottom). From left to right, the tensor shown is linear degenerate, linear non-degenerate, neutral, planar non-degenerate, and planar degenerate, respectively. Our glyphs are based on the deviators, which highlight the difference and symmetry between linear, neutral, and planar tensors. Green and red represent linear and planar, respectively. The colored bands on the glyph's *faces* correspond to eigenvalues with the same sign (two negative, in the case of linear tensors, and two positive for planar tensors). The direction perpendicular to the bands are the non-degenerate eigenvectors, i.e., major eigenvectors for linear tensors (green) and minor eigenvectors for planar tensors (red).

using glyphs and hyperstreamlines following any of the eigenvector fields. Furthermore, we extract the isosurfaces for tensor mode, tensor isotropy index, and tensor magnitude. All of these surfaces are extracted using the *A-patches* methods.

Degenerate curves are rendered as tubes around the actual degenerate curves. This makes it easier to perceive the absolute and relative depth of the degenerate curves. A point **p** on a degenerate curve γ can be further colored, based on the trace, tensor magnitude, and determinant as well as its linearity/planarity: green (linear) and yellow (planar). Traceless surfaces, neutral surfaces, as well as isosurfaces of the tensor mode, the magnitude, and the isotropy index are drawn using the smoke surface method [30]. To distinguish between them, we show isosurfaces of tensor modes (including the neutral surfaces) in the chartreuse color, the isosurfaces of the tensor isotropy index (including traceless surfaces) purple, and the isosurfaces of the tensor magnitude in cyan.

We have developed a set of glyphs that are designed for traceless tensors. Unlike existing glyph designs for indefinite tensors [17], [18] which employ both convex and concave glyph shapes, our approach only uses convex shapes. This is motivated by a number of needs from the domain users:

1) to highlight the location and eigenvector directions of neutral tensors.
2) to help emphasize the special eigenvector directions in degenerate tensors and make it easier to distinguish them from other eigenvectors.
3) to convey the symmetry between linear tensors and planar tensors, thus conveying once again the importance of neutral tensors.
4) to show the magnitude of tensor mode.

Consequently, we provide three glyph types: (1) degenerate tensors, (2) neutral tensors, and (3) non-degenerate and non-neutral tensors. Fig. 5 illustrates each glyph we use. A degenerate tensor is a cylinder where the axis of the cylinder indicates the non-degenerate eigenvector direction. A loop is drawn in the middle of the cylinder, circling this axis. The cylinder is color-coded in green if it is a linear degenerate tensor, and in red if it is a planar degenerate tensor. A neutral tensor is drawn as a flat disk with a color of gray, and the normal to the disk indicates the medium eigenvector direction. A red loop is drawn perpendicular to the minor eigenvector

direction, and a green loop is drawn perpendicular to the major eigenvector direction. For a non-degenerate, non-neutral tensor, we use a box with rounded corners and edges. The color of the box is green if it is linear, and red if planar. A loop is drawn at the middle of the faces of the box perpendicular to the non-degenerate eigenvector direction. Notice that the glyphs are designed to have continuity. For example, starting from a degenerate tensor (a cylinder) and decreasing tensor mode, the cylinder will morph into a box with round corners and edges. Eventually, it becomes a flat disk, i.e., middle image of the bottom row in Fig. 5. We wish to emphasize that we do not intend to replace existing, well-accepted glyph designed with our own. Instead, we consider our design a complementary approach.

7 APPLICATIONS

Performance. We have applied our analysis to a number of well-known data sets. The data is collected from a computer with an Intel Core i7 3.07 GHz processor, 24 MB of RAM, and an NVIDIA GTX Titan graphics card. The running time for our CPU-based feature (curves and surfaces) extraction algorithms is between 40 to 120 seconds.

Two fundamental quantities in solid and fluid mechanics are the stress and strain tensors. How the solid material deforms determines the design and performance of bridges, automobiles, circuit boards and medical devices that are investigated with the theories of solid mechanics. Being able to visualize the topology of the stress tensors can shed light on the force distribution. In fluid mechanics, one often studies the instantaneous velocity field and its spatial gradient. Such a gradient is asymmetric in general. The symmetric part of this velocity-gradient tensor is assumed to be proportional to the deviatoric stress tensor. This is the hypothesis for Newtonian fluid mechanics.

For a stress tensor, the eigenvectors indicate principal stress directions. The eigenvalues indicate the stress magnitude in these directions. The trace is three times the mean normal stress, while the determinant is the total volumetric change for the displacement gradient tensors, when the stress is proportional to the strain. The anisotropy in the tensor is measured by the relative strengths of the eigenvalues. For example, in medical imaging, researchers often classify the diffusion tensors into three types, linear, planar, and spherical, based on the eigenvalues.

In this paper, we focus on indefinite tensors such as the stress and strain tensors from solid and fluid mechanics. Stress tensors are symmetric which we can prove by calculating the angular momentum for an infinitesimal material volume. The degenerate curve indicates either tensile stress (linear) represented by the major eigenvalue or compressive stress (planar) represented by the minor eigenvalue on the material. Consequently, the linear domain and the planar domain express tension dominant (i.e., only one positive eigenvalue with the largest magnitude) and compression dominant regions (i.e., only one negative eigenvalue with the largest magnitude), respectively. On the neutral surfaces, the stress field becomes two dimensional, i.e., no deviatoric stress on one of the principal directions.

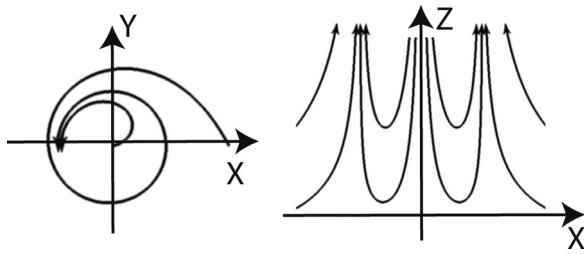Below we show results of our techniques applied to two applications.

Fig. 6. The Sullivan Vortex viewed in the x-y plane (left) and the x-z plane (right).

Fig. 7. Two geometric configurations of a linear elastic block being pressed from above by solid spheres.

7.1 Sullivan Vortex

The Sullivan vortex [31] is an exact analytical solution of the Navier-Stokes equations for incompressible fluids, whose flow patterns in the horizontal and vertical planes are depicted in Fig. 6. Away from the vortex center, the flow is predominantly in the negative radial direction (toward the center) with the upward flow. Near the center, the flow is outward with the down-welling motion. Note that the local flow pattern near the center resembles that of a hurricane or a tornado. To extract the symmetric part of the velocity-gradient tensor of the Sullivan vortex, we first compute $\frac{\nabla u + (\nabla u)^T}{2}$ in which u is the velocity vector: this tensor represents the time rate of angular deformation (i.e., the rate-of-strain tensor), and is traceless because of the assumption of incompressible fluids, i.e., $\lambda_1 + \lambda_2 + \lambda_3 = 0$. Even though the volume of the fluid particles are not changing, we call that the fluid parcels are predominantly compression when $\lambda_1 > 0$ and $\lambda_2 > 0$, while they are predominantly expansion when $\lambda_2 < 0$ and $\lambda_3 < 0$.

Fig. 1 shows (a) the velocity vector field and (b) the glyph presentation of the symmetric tensor field for the half domain that is cut vertically through the center, and (c) the degenerate curves with the neutral surface. Fig. 10 shows the glyph presentations in the horizontal cut planes at the mid-level and at the bottom of the domain, respectively. The figure also includes the location of the neutral surface on the cut planes. The visualization of the velocity vector field (Fig. 1a) shows the up-welling and down-welling motions. Additional information can be extracted from the glyph plot. In the outermost part in the plot in Fig. 1b (in the region far from the center of the vortex), the fluids are compressed in the horizontal direction, presented by the red glyphs (the planar type) with the red band oriented in the radial direction. The glyph presentation in the horizontal cut plane at the midlevel (Fig. 10 (top)) explicitly shows that the orientation of the minor eigenvector is in the clockwise spiral direction toward the center. At the level very close to the bottom (Fig. 10 (bottom)), the pattern is consistent with that at the midlevel, but they are closer (but not exactly) to the degenerate state. Across the outer neutral surface, the pattern of glyphs transforms to the green color (the linear type) pointing in the vertical direction (the green band around the glyphs are vertically oriented). The glyphs in the cut planes (Fig. 10 (top and bottom)) indicate the eigenvalues in the azimuthal direction are very small: the condition close to the neutral state. Across another neutral surface, fluid deformation takes place primarily in the x-z plane in the further inward and upper region away from the ground (Fig. 1b): the red glyph orientation in the region
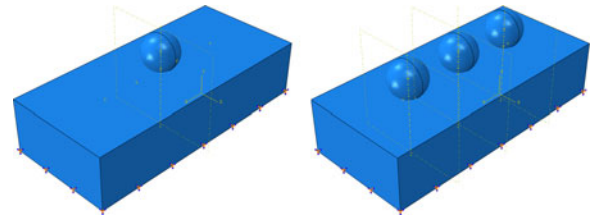
inside of the green band in Fig. 10 shows the eigenvalues in the azimuthal direction are small. Furthermore, fluids stretch vertically downward toward the center and compressing vertically upward toward the center (see the green and red band loop orientations in Fig. 1b). Near the ground level of the vortex center, the fluid deformation becomes complex, but is dominated by compression in the counter-clockwise spiral direction toward the center, which is opposite to the pattern of the outer region. Furthermore, we see the degenerate glyphs that correspond to the degenerate curves (yellow) shown in Fig. 1b: the planar degenerate curves that represent pure compression in the direction represented by the glyph orientations and the other eigenvectors being undefined: note that the direction of pure compression does not coincide with the tangential direction of the degenerate curve. The structure of degenerate curves for the Sullivan Vortex is further discussed next.

Fig. 1c presents the degenerate curves of the rate-of-strain tensor field. There are two distinct vertical planar type (yellow) lines surrounded by the two planar-type circular degenerate loops and the one linear circular degenerate loop (green). The two larger loops (the planar and linear types) are very close to the bottom boundary. The vertical planar degenerate curves represent the fluid compression due to the down-welling flow motion, which can be identified as the degenerate glyphs (red cylindrical shape) between the second and third neutral surfaces shown in Fig. 10b. As discussed earlier, the direction of the pure compression is not aligned with the (yellow) degenerate curve, but deviated in the counterclockwise spiral direction toward the center. Fig. 10b also shows the linear-type degenerate curve between the two inner neutral surfaces. The linear degenerate glyphs reveal that the stretching orientation is closely tangential to the degenerate curve. The successive linear type and planar type degenerate loops near the ground represent the fluid deformation (pure expansion near the center followed by pure compression away from the center). Note that the neutral surfaces shown in the transparent chartreuse color separate the linear type from the planar domain (Fig. 1c). The outer annular neutral surfaces coincide with the location of the cylindrical wall-like region of the linear type (green) shown in Fig. 1b. The transition pattern of the mode surfaces shown in Fig. 9 explicitly illustrates the flow kinematics associated with the Sullivan vortex, i.e., compression and expansion dominated deformations of the fluid parcels. Without the present tensor field visualization, such information is difficult to capture even for the simple flow like the Sullivan vortex.

The interplay of the small planar-type degenerate loop above the floor with the two vertical planar degenerate curves is worth noting. First, the glyphs in Fig. 1 indicate that the direction of eigenvector of λ_3 (compression) along
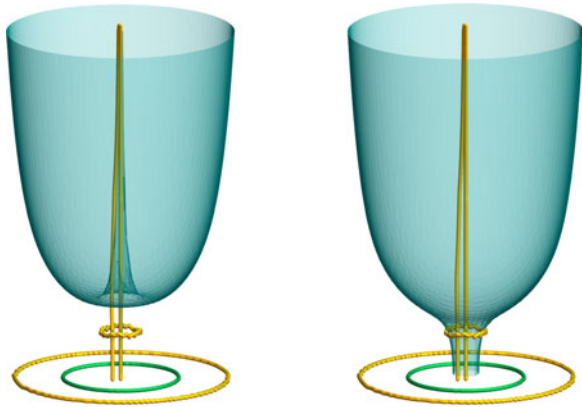
Fig. 8. This figure shows the degenerate curves in the Sullivan vortex in connection with its magnitude surfaces. Left and right, the isovalues of the magnitude surfaces are 15.44 and 13.79, respectively. Notice that the surface in the left is tangent to the vertical degenerate curves (yellow). In the center regions in both figures, the topology of the magnitude surface changes so that it is now tangent to the smallest degenerate loop (yellow). While the shape of the magnitude surfaces can be predicted based on the definition of the Sullivan vortex, their interesting interplay with the degenerate curves was not known to the best of our knowledge.

the degenerate loop is nearly vertical, slightly pointing upward toward the center. The iso-magnitude surfaces shown in Fig. 8 demonstrate that the small degenerate loop plays a role in the topology of the magnitude surface. Those topological features enable us to analyze the detailed and complex flow kinematics that appear in the relatively simple flow field of the Sullivan vortex.

We emphasize that the velocity gradient tensor of incompressible fluids is traceless. Consequently, it does not help to compute isosurfaces of the tensor isotropy index.

7.2 Spheres Compressing Linear Elastic Block

In the second application we include a solid mechanics example of a block deformed by spheres pressing on top (Fig. 7). We consider two scenarios with increasing complexity, and in our visualization, the spheres and the block themselves are omitted to accentuate the feature-based and topological surfaces. These numerical examples are extracted from research involving vehicle loading on roads and bridges.

We first apply the isosurfaces of the tensor isotropy index (not applicable to incompressible fluids) to the stress tensors
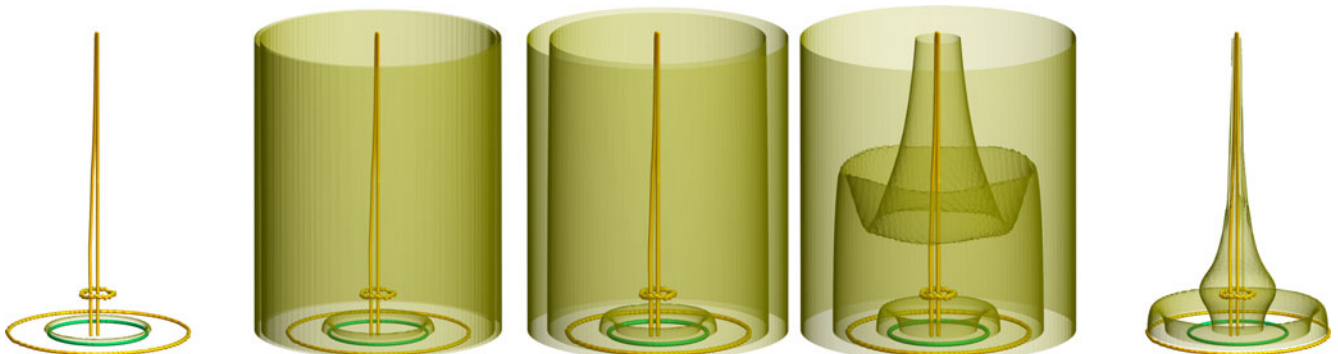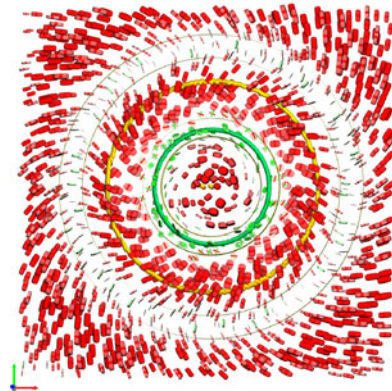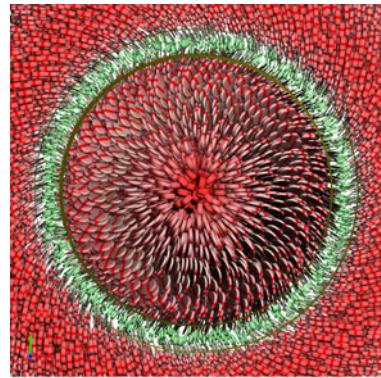

Fig. 10. Glyphs based on eigenvalue manifold in the horizontal cut plane at the midlevel (top) and at the bottom (bottom) of the Sullivan Vortex. The thin circular curves in chartreuse represent the intersect of neutral surface onto the cut plane, and the planar- and linear-type degenerate curves are shown with the thick lines in yellow and green, respectively.

for the one sphere case. In Fig. 11, we show that while the isotropy index varies from 0.70 to -0.70, the zones with shear stress grow and then shrink similar to the behavior analogous to the vertical bisector of the lune.

The combination of the traceless surface and the mode surface of this dataset is shown in Fig. 12 (1a and 1b: neutral surfaces in chartreuse and traceless surfaces in purple). The left column shows an angle view and the middle row a side view. Notice that both surfaces reveal the indentation, the hollow area in the middle, made by the sphere. In addition, the neutral surface and the traceless surface are both mostly aligned with the top face of the block, implying that the behaviors of
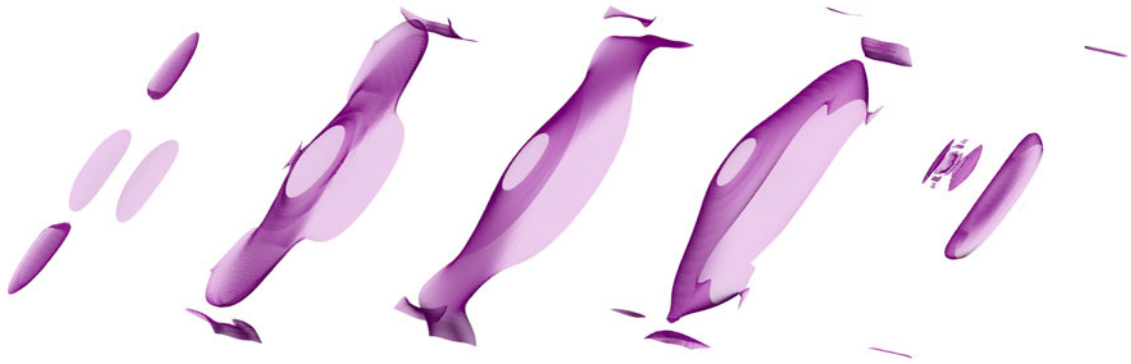

Fig. 9. The mode surfaces of the Sullivan vortex (Fig. 1). From left to right, the mode values are 0.8, 0.4, 0 (the neutral surface), -0.4, and -0.94, respectively. Notice that the linear degenerate curves (green) and the planar degenerate curves (yellow) are separated by the neutral surface. Moreover, the topology of the mode surface changes. As the mode increases, the mode surfaces converge toward linear degenerate curves. In contrast, when the mode decreases, the mode surfaces converge toward planar degenerate curves.

Fig. 11. The isosurfaces of the isotropy index with values at 0.70, 0.36, 0, −0.36, and −.70 for the single sphere scenario in Fig. 7.

the materials are nearly uniform, i.e., vertical compression. It is interesting to note that the neutral surface (two layers) sandwich the traceless surface. This is an observation that can lead to further investigations by material scientists. Typically, engineers who evaluate the stress distribution are limited to plotting the von Mises stress, which presents a high-low magnitude of the deviatoric stress and is insufficient in tracking the displacement of the material. The traceless surfaces separate the important zones of material layers which are in expansion and compression, and this division can facilitate creation of designs that incorporate multi-materials and sensors. By viewing the neutral surfaces, investigation can evolve in correlating the eigen-directions to material displacement. This information enables intelligent and optimal definition of boundary conditions for the materials. Furthermore, in the three sphere (bottom row) scenario (Fig. 12), we note that between every pair of adjacent spheres, a tubular region emerges underneath. The neutral tensors enclose these

tubular regions, an observation that shows the material being compressed by the pair of spheres and is pushed to the sides, changing from planar compression to linear compression while crossing the neutral surfaces. The capability of isolating these regions is new to the best of our knowledge. We wish to point out that the tensor mode surfaces, including the neutral surfaces, do not possess global self-intersections. While this is hard to see in Fig. 12 (lower-middle), it is more discernable from another viewpoint (Fig. 13).

7.3 Scalar Field Analysis

The Hessian of a smooth scalar field is a 3×3 symmetric tensor field, containing its partial second derivatives. Examples in which Hessians were previously used in scalar field visualization include the classification of critical points when constructing Morse-Smale complexes [32], or the definition of curvature-based transfer functions for direct volume rendering [33].

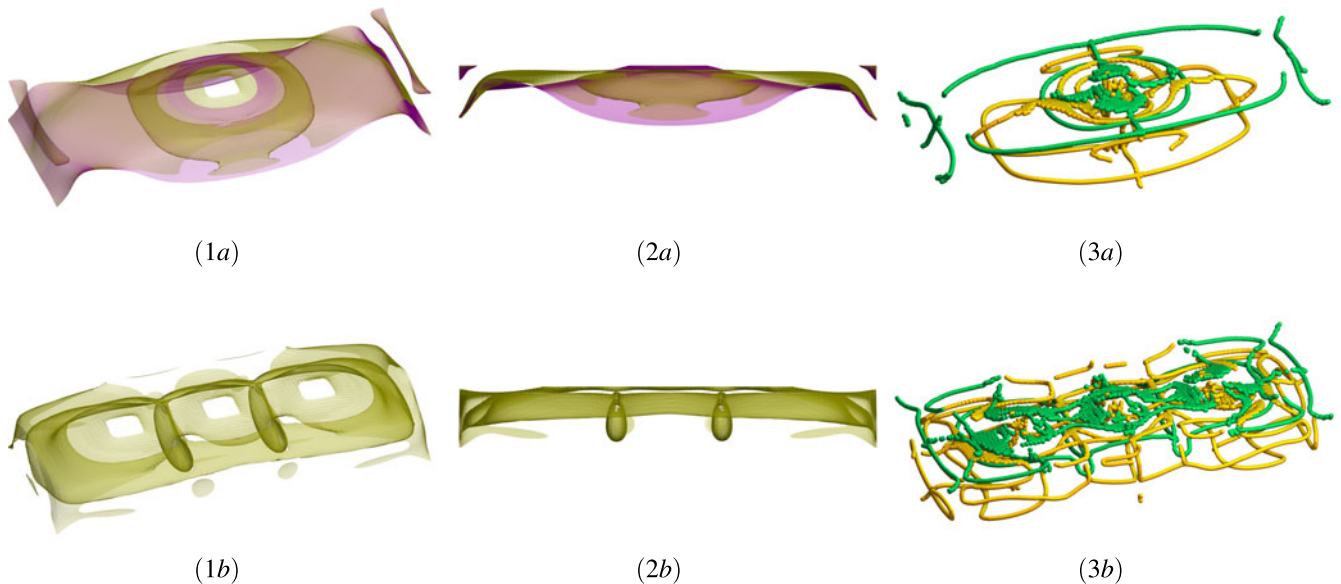

(1a) (2a) (3a)

(1b) (2b) (3b)

Fig. 12. This figure shows the neutral surfaces (left and middle columns) and degenerate curves (right column) for two scenarios of spheres pressing a block. The left column shows an angled view and the middle column shows a side view. In the top row, we also show the traceless surface. We note the two surfaces are nearly parallel generally following the shape of the block. In addition, the neutral surface has two sheets which sandwich one sheet of the traceless surface. Above the traceless surface is the region of expansion while below the traceless surface is the region of contraction. The expansion region is linear above the upper sheet of the mode surface and planar below it. The bottom row shows a tubular region emerging beneath pairs of spheres for the three sphere scenarios. These regions indicate planar tensors. In addition, the trace in those regions are negative, indicating compression. However, the compression is not isotropic. There is one direction with the most compression while the other two directions exhibit less compression (or even with slight extension). In the right column, the degenerate curves for one sphere and three spheres are shown, respectively. Notice that the linear degenerate curves and planar degenerate curves are separate from each other in the one sphere case. However, for three spheres, the two types can interact through links (green curves linking yellow curves).

Fig. 13. The neutral surface is the zeroth levelset of the tensor mode function and has no self-intersections. While this can be difficult to perceive given our choice of surface rendering [30] when there are multiple layers in the surface (e.g., Fig. 12-1b), viewing the dataset from different angles (e.g., this figure) can clarify this. Notice that in this figure there is clearly a separation between the outermost part of the neutral surface and the next layer, which is difficult to judge from the top figure.

Applying our newly proposed method for tensor field analysis to Hessians allows us to use it to gain insight into scalar fields. For example, a classic method for edge detection in volumetric scalar data involves localizing the Laplacian zero crossings [34], which coincide with the traceless surfaces in our framework. Similarly, Schultz et al. [35] point out that generic height ridge and valley surfaces end in degenerate curves of the Hessian field briefly before they form a junction. Thus, neutral surfaces partition the domain into parts in which ridge surfaces (negative mode) or valley surfaces (positive mode) can form such a configuration.
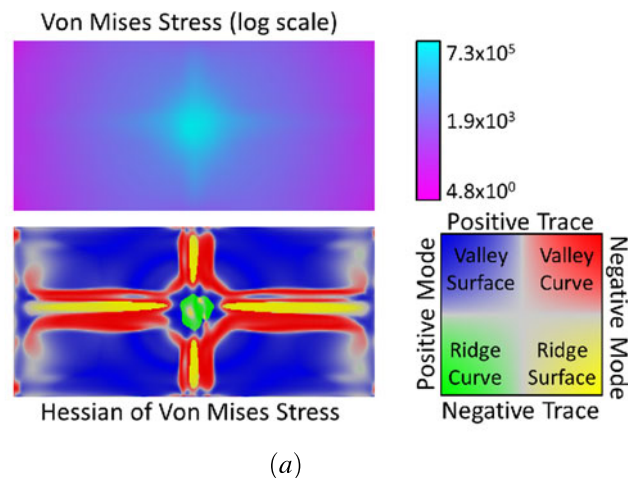
Fig. 14 shows the neutral (b) and traceless (c) surfaces in the Hessian of the von Mises stress, a scalar field that is derived from the one-sphere simulation. We have found that these surfaces reveal interesting structures that are complementary to those in the stress tensor field itself (Fig. 12, top row). Together, neutral and traceless surfaces lead to a four-way partitioning of the domain. Fig. 14a illustrates it using a color coding on a slice that is located near the top of the block, oriented perpendicular to the external force. This subdivision clearly reflects the main maximum of the Von Mises stress (green) and the ridges leading up to it (yellow).

In general, positive Hessian trace indicates a region in which the scalar field is concave (including all local minima), while negative trace indicates convexity (local maxima). The mode of the Hessian tensor is affected by the dimensionality of the local extremum. For example, Hessians along a typical valley line have negative tensor mode, with two clearly positive eigenvalues, and a remaining less dominant one. In contrast, a planar valley surface is characterized by a single dominant positive eigenvalue, leading to positive tensor mode. As indicated in the legend of Fig. 14a, the roles of positive and negative mode are reversed in case of ridges.

8 CONCLUSION AND FUTURE WORK

In this paper, we have presented novel analysis of 3D symmetric tensor fields. At the core of our approach is the introduction of the eigenvalue manifold for 3D tensors, as well as the neutral surfaces and traceless surfaces and their inclusion into tensor field analysis. We have also defined the concept of tensor isotropy index which, along with tensor mode, are used to parameterize the eigenvalue manifold.
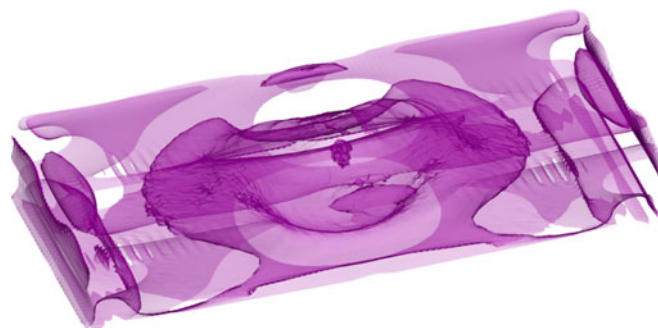
We make use of the *A-patches* method to efficiently extract mode surfaces (including the neutral surfaces) and the isotropy index surfaces (including the traceless surfaces). Finally, we provide physical interpretation of our analysis and visualization in the context of fluid dynamics and

(a)

(b)

(c)

Fig. 14. This figure shows that tensor field analysis can also be useful for scalar field visualization. Given a 3D scalar field (a: top), which is the von Mises stress for the one-sphere simulation data in Fig. 7 (left), the Hessian is a symmetric tensor field which can contain rich structures (a (bottom), b and c) and provide critical and complementary information about the original scalar field.

solid mechanics. We also demonstrate that our analysis can be applied to scalar field visualization.

Our system is not without limitations. Our system does not guarantee that all degenerate curves and neutral surfaces are extracted. This can be attributed to the fact that the *A-patches* algorithm that we adapted [6] does not guarantee convergence when there are singularities on the surfaces, like cusps.

Like scalar and vector fields, noise and numerical issues can lead to noise in tensor field analysis. As a future

direction, we plan to investigate techniques to reduce geometric and topological noise in tensor field analysis. Furthermore, extending our analysis to 3D asymmetric tensor fields is also a natural direction. Finally, we wish to explore means to reduce the visual cluttering associated with displaying degenerate curves and neutral surfaces.

ACKNOWLEDGMENTS

REFERENCES

[1] X. Zheng and A. Pang, "Topological lines in 3d tensor fields," in *Proc. IEEE Vis.*, 2004, pp. 313–320.
[2] X. Zheng, B. N. Parlett, and A. Pang, "Topological lines in 3d tensor fields and discriminant hessian factorization," *IEEE Trans. Vis. Comput. Graph.*, vol. 11, no. 4, pp. 395–407, Jul. 2005.
[3] X. Zheng, B. Parlett, and A. Pang, "Topological structures of 3D tensor fields," in *Proc. IEEE Vis.*, 2005, pp. 551–558.
[4] X. Tricoche, G. Kindlmann, and C.-F. Westin, "Invariant crease lines for topological and structural analysis of tensor fields," *IEEE Trans. Vis. Comput. Graph.*, vol. 14, no. 6, pp. 1627–1634, Nov./Dec. 2008.
[5] G. M. Treece, R. W. Prager, and A. H. Gee, "Regularised marching tetrahedra: Improved Iso-surface extraction," *Comput. Graph.*, vol. 23, pp. 583–598, 1998.
[6] C. Luk and S. Mann, "Tessellating algebraic curves and surfaces using A-patches," in *Proc. 4th Int. Conf. Comput. Graph. Theory Appl.*, 2009, pp. 82–89.
[7] E. Zhang, J. Hays, and G. Turk, "Interactive tensor field design and visualization on surfaces," *IEEE Trans. Vis. Comput. Graph.*, vol. 13, no. 1, pp. 94–107, Jan./Feb. 2007.
[8] E. Zhang, H. Yeh, Z. Lin, and R. S. Laramee, "Asymmetric tensor analysis for flow visualization," *IEEE Trans. Vis. Comput. Graph.*, vol. 15, no. 1, pp. 106–122, Jan./Feb. 2009.
[9] D. K. Jones, Ed., *Diffusion MRI: Theory, Method, and Applications*. London, U.K.: Oxford Univ. Press, 2011.
[10] T. Schultz, "Feature extraction for DW-MRI visualization: The state of the art and beyond," in *Proc. Scientific Vis.: Interactions, Features, Metaphors*, 2011, vol. 2, pp. 322–345.
[11] A. Kratz, C. Auer, M. Stommel, and I. Hotz, "Visualization and analysis of second-order tensors: Moving beyond the symmetric positive-definite case," *Comput. Graph. Forum*, vol. 32, no. 1, pp. 49–74, 2013.
[12] G. Scheuermann and X. Tricoche, "Topological methods in flow visualization," in *Visualization Handbook*, C. Hansen and C. Johnson, Eds. Amsterdam, The Netherlands, Elsevier, 2005, pp. 341–358.
[13] T. Delmarcelle and L. Hesselink, "Visualizing second-order tensor fields with hyperstream lines," *IEEE Comput. Graph. Appl.*, vol. 13, no. 4, pp. 25–33, Jul. 1993.
[14] E. Hsu, "Generalized line integral convolution rendering of diffusion tensor fields," in *Proc. 9th Sci. Meeting Exhib. Int. Soc. Magnetic Resonance Med.*, 2001, p. 790.
[15] X. Zheng and A. Pang, "Hyperlic," in *Proc. IEEE Vis.*, 2003, pp. 249–256.
[16] B. Cabral and L. C. Leedom, "Imaging vector fields using line integral convolution," in *Poc. ACM SIGGRAPH 1993*, 1993, pp. 263–272.
[17] T. J. Jankun-Kelly and K. Mehta, "Superellipsoid-based, real symmetric traceless tensor glyphs motivated by nematic liquid crystal alignment visualization," *IEEE Trans. Vis. Comput. Graph.* vol. 12, no. 5, pp. 1197–1204, Sep. 2006.
[18] T. Schultz and G. L. Kindlmann, "Superquadric glyphs for symmetric second-order tensors," *IEEE Trans. Vis. Comput. Graph.*, vol. 16, no. 6, pp. 1595–1604, Nov./Dec. 2010.
[19] T. Delmarcelle and L. Hesselink, "The topology of symmetric, second-order tensor fields," in *Proc. IEEE Conf. Vis.*, 1994, pp. 140–147.
[20] L. Hesselink, Y. Levy, and Y. Lavin, "The topology of symmetric, second-order 3D tensor fields," *IEEE Trans. Vis. Comput. Graph.*, vol. 3, no. 1, pp. 1–11, Mar. 1997.
[21] T. Schultz, H. Theisel, and H.-P. Seidel, "Topological visualization of brain diffusion MRI data," *IEEE Trans. Vis. Comput. Graph.*, vol. 13, no. 6, pp. 1496–1503, Nov. 2007.
[22] R. Peikert and M. Roth, "The parallel vectors operator-a vector field visualization primitive," in *Proc. Visualization*, Oct. 1999, pp. 263–532.
[23] C. Dick, J. Georgii, R. Burgkart, and R. Westermann, "Stress tensor field visualization for implant planning in orthopedics," *IEEE Trans. Vis. Comput. Graph.*, vol. 15, no. 6, pp. 1399–1406, Nov./Dec. 2009.
[24] A. Kratz, M. Schoeneich, V. Zobel, B. Burgeth, G. Scheuermann, I. Hotz, and M. Stommel, "Tensor visualization driven mechanical component design," in *Proc. IEEE Pacific Vis. Symp.*, 2014, pp. 145–152.
[25] J. Damon, "Generic structure of two-dimensional images under gaussian blurring," *SIAM J. Appl. Math.*, vol. 59, no. 1, pp. 97–138, 1998.
[26] L. Markus. (1955). Line element fields and lorentz structures on differentiable manifolds. *Ann. Math.* [Online]*62(3)*, pp. 411–417 Available: http://www.jstor.org/stable/1970071
[27] S. Kazimi, *Solid Mechanics*. New York, NY, USA: McGraw-Hill, 1982.
[28] J. J. Koenderink and A. J. van Doorn, "Surface shape and curvature scales," *Image Vis. Comput.*, vol. 10, no. 8, pp. 557–565, Oct. 1992.
[29] M. Nieser, J. Palacios, K. Polthier, and E. Zhang, "Hexagonal global parameterization of arbitrary surfaces," *IEEE Trans. Vis. Com1put. Graph.*, vol. 18, no. 6, pp. 865–878, Jun. 2012.
[30] W. von Funck, T. Weinkauf, H. Theisel, and H.-P. Seidel, "Smoke surfaces: an interactive flow visualization technique inspired by real-world flow experiments," *IEEE Trans. Vis. Comput. Graph.*, vol. 14, no. 6, pp. 1396–1403, Nov. 2008.
[31] R. D. Sullivan, "A two-cell vortex solution of the Navier-Stokes equations," *J. Aero/Space Sci.*, vol. 26, no. 11, pp. 767–768, Nov. 1959.
[32] H. Edelsbrunner, J. Harer, V. Natarajan, and V. Pascucci, "Morse-smale complexes for piecewise linear 3-manifolds," in *Proc. 19th Annu. Symp. Comput. Geom.*, 2003, pp. 361–370.
[33] G. Kindlmann, R. Whitaker, T. Tasdizen, and T. Möller, "Curvature-based transfer functions for direct volume rendering: methods and applications," in *Proc. IEEE Visualization*, 2003, pp. 513–520.
[34] D. Marr and E. Hildreth, "Theory of edge detection," *Proc. Roy. Soc. London. Series B, Biol. Sci.*, vol. 207, no. 1167, pp. 187–217, 1980.
[35] T. Schultz, H. Theisel, and H.-P. Seidel, "Crease surfaces: from theory to extraction and application to diffusion tensor MRI," *IEEE Trans. Vis. Comput. Graph.*, vol. 16, no. 1, pp. 109–119, Jan./Feb. 2010.

Jonathan Palacios received the PhD degree in computer science in 2015 from Oregon State University. His primary research areas are computer graphics, geometric modeling, symmetry, and higher-order tensor field visualization and analysis. He was an US National Science Foundation (NSF) IGERT fellow, and is a member of the ACM.

Harry Yeh received the PhD degree in civil engineering in 1983 from the University of California, Berkeley. His research interests are in the areas of environmental fluid mechanics, water wave phenomena, wind turbulence, and tsunami hazard mitigation. He was a hydraulic engineer at Bechtel Inc., San Francisco from 1977 to 1983. From 1983 to 2002, he was a professor at the University of Washington, Seattle. He is currently the Edwards chair professor in engineering at Oregon State University.

Wenping Wang received the BSc and MEng degrees in computer science from Shandong University, China, in 1983 and 1986, respectively, and the PhD degree in computer science from the University of Alberta, Canada, in 1992. He is currently a professor of computer science at the University of Hong Kong, China. His research interests include computer graphics, geometric computing, and computational geometry.

Yue Zhang received the PhD degree in computational mathematics in 1997 from North Carolina State University. From 1997 to 2011, she worked for Michelin North American Research and Development Company as a Tire simulation researcher. She is currently an assistant professor senior research in the School of Electrical Engineering and Computer Science at Oregon State University. Her research interests are in physics-based simulation, computer graphics, and scientific visualization. She is a member of the IEEE.

Robert S. Laramee received the bachelors degree in physics, cum laude, from the University of Massachusetts, Amherst (Zoo Mass) and the masters degree in computer science from the University of New Hampshire, Durham, and the PhD degree from the Vienna University of Technology, Austria at the Institute of Computer Graphics and Algorithms in 2005 (Gruess Gott TUWien). From 2001 to 2006, he was a researcher at the VRVis Research Center (www.vrvis.at) and a software engineer at AVL (www.avl.com) in the Department of Advanced Simulation Technologies. Currently he is an associate professor at the Swansea University (Prifysgol Cymru Abertawe), Wales in the Department of Computer Science. His research interests are in the areas of scientific visualization, information visualization, and visual analytics. He is a member of the IEEE.

Ritesh Sharma received the bachelor's degree in computer science and engineering from the West Bengal University of Technology. He is a master of science student in the school of Electrical Engineering and Computer Science at Oregon State University. He is working with Dr. Eugene Zhang on Tensor Field Visualization. Prior to enrolling at Oregon State University, he worked for three years as research assistant at the Indian Institute of Technology, Bombay. His current research interests include the areas of computer graphics, computational geometry, and scientific visualization.

Thomas Schultz received the doctoral degree in computer science in 2009 from Saarland University, for work done at the Max Planck Institute in Informatics, Germany. From 2009 to 2011, he spent two years as a DAAD postdoctoral fellow at the University of Chicago. From 2011 to 2014, he worked as a research scientist at the Max Planck Institute in Intelligent Systems in Tübingen, Germany. Since 2013, he has been a junior professor in computer science at the University of Bonn, Germany, working on visualization and medical image analysis.

Eugene Zhang received the PhD degree in computer science in 2004 from the Georgia Institute of Technology. He is currently an associate professor at Oregon State University, where he is a member of the School of Electrical Engineering and Computer Science. During part of 2011 and 2012, he was a guest professor at the Free University of Berlin and the Max-Planck-Institute in Informatics. His research interests include computer graphics, scientific visualization, geometric modeling, and computational topology. He received an National Science Foundation (NSF) CAREER award in 2006. He is a senior member of both the IEEE and the ACM.

▷ **For more information on this or any other computing topic, please visit our Digital Library at** www.computer.org/publications/dlib.